Ferromagnetism in Co-doped ZnO films grown by molecular beam epitaxy: magnetic, electrical and microstructural studies

V.V. Strelchuk,[1] V.P. Bryksa,[1] K.A. Avramenko,[1] P.M. Lytvyn,[1] M.Ya. Valakh,[1]
V.O. Pashchenko,[2] O.M. Bludov,[2] C. Deparis,[3] C. Morhain,[3] and P. Tronc[4]

[1] *V. Lashkaryov Institute of Semiconductor Physics National*
Academy of Sciences of Ukraine, 45 Nauky pr., 03028 Kyiv, Ukraine
[2] *B. Verkin Institute for Low Temperature Physics and Engineering National*
Academy of Sciences of Ukraine, 47 Lenin Ave., 61103 Kharkiv, Ukraine
[3] *Centre de Recherches sur l'Hétéroépitaxie et ses Applications, CNRS, F-06560 Valbonne, France*
[4] *Centre National de la Recherche Scientifique, Ecole Superieure de Physique et de*
Chimie Industrielles de la Ville de Paris, 10 rue Vauquelin, 75005 Paris, France
(Dated: January 15, 2013)

We studied structural, optical and magnetic properties of high-quality 5 and 15% Co-doped ZnO films grown by plasma-assisted molecular beam epitaxy (MBE) on (0001)-sapphire substrates. Magnetic force microscopy (MFM) and magnetic measurements with SQUID magnetometer show clear ferromagnetic behavior of the films up to room temperature whereas they are antiferromagnetic below 200 K approximately. Temperature dependence of the carrier mobility was determined using Raman line shape analysis of the longitudinal-optical-phonon-plasmon coupled modes. It shows that the microscopic mechanism for ferromagnetic ordering is coupling mediated by free electrons between spins of Co atoms. These results bring insight into a subtle interplay between charge carriers and magnetism in MBE-grown $Zn_{1-x}Co_xO$ films.

I. INTRODUCTION

Currently one can observe a great interest in understanding and designing the physical properties of diluted-magnetic-semiconductor (DMS) structures. Indeed, they have potential applications in spintronics, where controlling electron spin can give rise to new devices. Since theoretical calculations predicted possible room-temperature ferromagnetism (FM)[1], in transition-metal-doped $Zn_{1-x}T_xO$ films ($T = Cr^{2+}$, Mn^{2+}, Fe^{2+}, Co^{2+} and Ni^{2+}) they attracted a great interest. Experimental observations of room-temperature FM in V^{2+}:ZnO[2], Fe^{2+}:ZnO[3], and Co^{2+}:ZnO[4] appeared in the literature. It seems reasonable to assume that FM is merely due to magnetic impurities, even if some experimental results appeared to rule this out[5]. At the present time, the microscopic mechanism responsible for high-T_c FM is still quite controversial for the II-VI compounds, especially for ZnO based DMSs[6]. Various mechanisms have been proposed for the bulk materials, for example, carrier-induced ferromagnetism[1] and percolation of bound magnetic polarons[7]. In addition, structural defects probably play significant role in controlling the ferromagnetic properties of the ZnO. The main reasons referred to in the literature for appearance of a ferromagnetic phase are substitution of Zn atoms by Co ones and existence of magnetic clusters of metallic Co and/or Co oxides in ZnO host. Furthermore, the magnetic properties of Co^{2+}:ZnO films have a strong dependence on synthesis and processing conditions[8]. In some cases, even the conclusion of intrinsic ferromagnetism remains controversial[8].

The ferromagnetic properties of $3d$-metal-doped ZnO nano-particles were explained using the core-shell model[9]. High stability of ferromagnetic phase in Ni^{2+}:ZnO nanocrystals was related to high surface-defect-concentration[10]. High-T_c ferromagnetism in Mn^{2+}:ZnO and Co^{2+}:ZnO nanocrystals was interpreted as a result of long-range exchange interaction of Mn^{2+} and Co^{2+} ions mediated by charge carriers[11]. The important role of magnetic anisotropy of Co^{2+} ions in ZnO lattice[12] has been discussed as well as clearly observed correlation between magnetism and carrier concentration in $Zn_{1-x}Co_xO$ films[13]. Nano-scale non-uniform distribution of magnetic ions in the host lattice and spinodal decomposition have recently been observed in Cr-doped $ZnSe$ films [14]. The films show ferromagnetic ordering with high values of the Curie temperature.

Three models have been proposed to explain room temperature ferromagnetism in $Zn_{1-x}Co_xO$ alloys. In the first one, ferromagnetism is mediated indirectly via free carriers (Ruderman-Kittel-Kasuya-Yoshida (RKKY) or double exchange mechanism model). In the second one, ferromagnetism originates from secondary phase such as metallic Co or Co-oxides. And the latter is due to the bound magnetic polaron model. In order to clarify this ambiguous situation, we studied MBE-grown $Zn_{1-x}Co_xO$ thin films with the help of magnetic force microscopy (MFM), confocal micro-Raman, photoluminescence (PL) and $SQUID$ techniques.

Raman scattering became a very useful and informative technique for studying different phonon excitations in undoped and doped by Li, N, Fe, Sb, Ga, Al ZnO films. It allows studying influence of structural disorder

in ZnO lattice on vibrational properties[15]. The study of $Co - O - Zn$ local vibration modes versus concentration of oxygen vacancies[16] allows correlating carrier concentration and magnetic properties. Appearance of phonon bands at 186, 491, 526, 628, and 718 cm^{-1} was interpreted as a signature of $Zn_yCo_{3-y}O_4$[17] spinel phase. Note, that nanometer-size $Zn_yCo_{3-y}O_4$ clusters can be very easily detected in micro-Raman measurements whereas X-ray diffraction method is not well-suited for studying so small clusters.

In the absence of magnetic secondary phases, the distribution of Co^{2+} ions over cation sites of ZnO lattice should play an important role for ferromagnetism. A substituting Co^{2+} ion at a Zn site can have no Co second first neighbor i.e., not to be involved in one (several) Co-O-Co sequence(s) or have at least one Co second neighbor. The magnetic properties have strong dependence on the number of Co atoms of the first type (isolated atoms). Assuming that Co atoms are randomly distributed over cation sites and neglecting antisite and interstitial-site occupation, it was shown for the 5 and 15%Co-doped ZnO films that 94 and 14% of Co atoms, respectively, belong to the first type. Note that the assumption rules out metallic Co clusters[8,18]. It is expected that isolated Co atoms have ferromagnetic interaction mediated by free carriers. In the $Co - O - Co$ bonding configurations, the two neighboring Co localized spins are assumed to be coupled antiparallel providing antiferromagnetic properties , especially at low temperature[8,18–21]. As a result there is a competition between the ferromagnetic and antiferromagnetic interactions in the $Zn_{1-x}Co_xO$ films. It is expected that ferromagnetic interactions between Co^{2+} ions should take place in high quality MBE-grown $Zn_{1-x}Co_xO$ films with high electron concentrations ($n > 10^{19}$ cm^{-3})[21].

The present paper is organized as follows. Section II describes the growth procedure and setup for micro-Raman, MFM and magnetic measurements. In Section III, we focus on the magnetic, structural, optical and electronic properties of the MBE-grown 5% and 15% Co-doped $Zn_{1-x}Co_xO$ thin films. Using the MFM and SQUID technique, the magnetic interactions in the films are determined. In the films a broad emission peak at 1.816 eV (683 nm) is put into evidence which is ascribed to electron transitions within substitional Co^{2+} ions. These results confirm that the Co^{2+} ions are located at the Zn sites in the wurtzite ZnO structure. The micro-Raman measurement confirms the crystalline wurtzite structure in Co-doped ZnO films. The temperature-dependent Raman measurements of longitudinal-optical-phonon-plasmon coupled modes (LOPCMs) are also provided. Modeling Raman spectra for the LOPCMs allows determining the temperature dependence of the carrier mobility. The results evidence that the ferromagnetism of the $Zn_{1-x}Co_xO$ films is due to the free carriers with high mobility and supports an indirect interaction of localized magnetic moments of isolated Co^{2+} ions in the ZnO lattice. Section IV is assigned to summary and outlook.

II. EXPERIMENTAL DETAILS

The $Zn_{1-x}Co_xO$ films were grown on c-sapphire substrates in a Riber Epineat MBE system equipment with conventional effusion cells for elemental Zn and Co. Atomic oxygen was supplied via an Addon radio-frequency plasma cell equipped with a high-purity quartz cavity[19]. The film thickness is about 1.7 μm. The epilayer crystalline quality is attested by low full-width-at-half-maximum values in high-resolution X-ray diffraction scans for high-symmetry as well as oblique directions (see Table I). Lattice parameters of the pure ZnO sample matches well with the values of ZnO single crystal ($a = 3.2495$ Å, $c = 5.2069$ Å). After Co substitution with Zn atom both a- and c-axis lattice constants are changed ($a = 3.266$ (3.259) Å and $c = 5.197$ (5.195) Å for 5 (15) at.% Co). Some discrepancy between the concentrations determined using contactless sub-micrometer Raman and macro-Hall measurements (Table I) can be caused by differences in local regions of measurements and possible changes of electric parameters due to heating under contact formation for Co-doped ZnO films.

TABLE I: Parameters of MBE growth for undoped and Co-doped of the ZnO films and determined values of the carrier mobility and concentrations obtained by Hall and Raman measurements at room temperature.

Sample number	226	283	288
Co concentration (%)	–	5	15
Growth rate (μm/hour)	0.66	0.43	0.43
Growth temperature (°C)	510	560	560
X-ray line FWHM (degree)	–	[002]: 0.29 [-105]: 0.28 [102]: 0.78 Twist: ±0.54	[002]: 0.32 [-105]: 0.21 [102]: 0.57 Twist: ±0.35
Mobility (cm^2/Vs) measured by			
Hall	32	47	29
Raman*	–	98	130
Electron density (cm^{-3}) measured by			
Hall	1×10^{18}	0.1×10^{20}	0.7×10^{20}
Raman*	–	1.2×10^{20}	1.3×10^{20}

* The accuracy of determining the carrier concentration from analysis of modelled ω^+ LOPCM was about ±20%.

Confocal micro-Raman and PL measurements were performed using the 488.0 nm line of the Ar^+/Kr^+ laser and recorded with a Jobin-Yvon $T64000$ spectrometer equipped with a CCD detector. Spatial resolution

(lateral and axial) was about 1 μm. The temperature-dependent micro-Raman spectra (80-500 K) were performed using a Linkam THM600 temperature stage.

The MFM measurements were performed by a Dimension 3000 Nano-Scope $IIIa$ scanning probe microscope for spatial mapping of the magnetization structure of the out-of-plane component of the magnetic stray field of the $Zn_{1-x}Co_xO$ sample surface at room temperature. Before measurements, the probe was magnetized using a strong permanent magnet with the field aligned along the tip axial axis. Then the MFM images of the sapphire substrate surface were taken and no magnetic signal was registered. The magnetic force gradients were measured using a two-pass technique (Lift Mode), where the topography was scanned at the first pass in the tapping mode and then the magnetic field gradients were obtained using oscillation frequency shift of the probe moving over surface. The cobalt coated Veeco magnetic tips with a coercivity of $\approx$ 400 Oe, magnetic moment of 1×10^{-13} emu and 25 nm nominal tip apex radius were used. The two opposite orientations of probe magnetization were used (i.e. North or South pole on the tip apex). This allows distinguishing the signal of the gradient magnetic fields from other artefacts of long-range electrostatic fields detected by the magnetic tip apex. The value of lift scan height was optimized for maximal sensitivity and minimal topography effects and was about 100 nm. The chip structure of $Zn_{1-x}Co_xO$ samples were also studied by using a ZEISS EVO-50 scanning electron microscope (SEM). The magnetic measurements were carried out using a Quantum Design SQUID magnetometer $MPMS-XL5$.

III. RESULTS AND DISCUSSION

AFM is used to characterize surface morphology, root-mean-square (rms) roughness, to verify the microstructures of $Zn_{1-x}Co_xO$ films. AFM morphology image of $Zn_{1-x}Co_xO$ films in the regions of chipped film edge changes with increase of the Co concentration (Fig. 1). As seen from Fig. 1(a), morphology of 5%-doped ZnO films is very tiny crystal grains $(20 - 30$ nm) due to the vertical columnar growth mode, and it shows the rms roughness of about 1.8 nm. For 15% Co-doped ZnO films (Fig. 1(b)) the rms roughness is close to 2 nm, the larger domain structures with sizes from 100 to 400 nm are formed by connecting smaller crystal grains. Let us note that in this case the smaller crystal grain size is practically unchanged with increasing Co concentration. Similar morphology was reported for the $Zn_{1-x}Co_xO$[22] and Al-doped ZnO[23] films.

The surface sensitive MFM method was used to study magnetization in the vicinity of the chipped sample edge of the Co-doped ZnO films. We deal with the area of pure substrate and sharp film edge (Fig. 2). As seen from the profiles (Fig. 2c), magnetization of the 15%Co-doped ZnO film, exhibits a sharp jump in magnetic signal at the chipped edge for the South and North pole of the probe
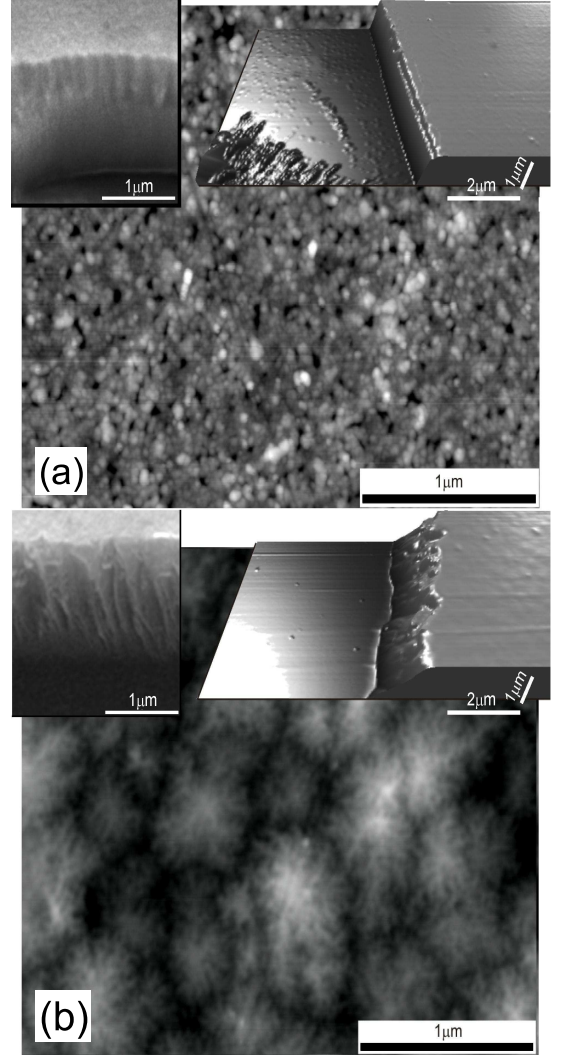

FIG. 1: 3×3 μm^2 AFM images for ZnO films doped with 5%(a) and 15%(b) on the sapphire substrate. On insert show 10×10 μm^2 SEM (left) AFM (right) images of the chipped edge.

(Fig. 2a,b). The MFM magnetization map is independent of the AFM topography image of the $Zn_{1-x}Co_xO$ surface films. For the 5%Co-doped ZnO film, similar changes in the MFM image take place, but changes are not so sharp, and their value is $\sim$ 10 times lower than for the 15%Co-doped ZnO film(Fig. 2c).

In the area of the film sharp edge, MFM probe interacts with the studied surface not only by the tip apex but by some area of side surface also, which causes local increase of the MFM signal amplitude. As shown on the Fig. 2c, magnetization of the $Zn_{1-x}Co_xO$ films for the South pole has a lower value when compared with that of the North pole. This fact can be explained by the hysteresis of the magnetic film (curves 1b(S) and 1a(N) on Fig. 2c) and agrees well with SQUID data at $T = 300$ K and $H \parallel c$ geometry in a magnetic field of $H_{MFM} \approx 15 Oe$ (insert
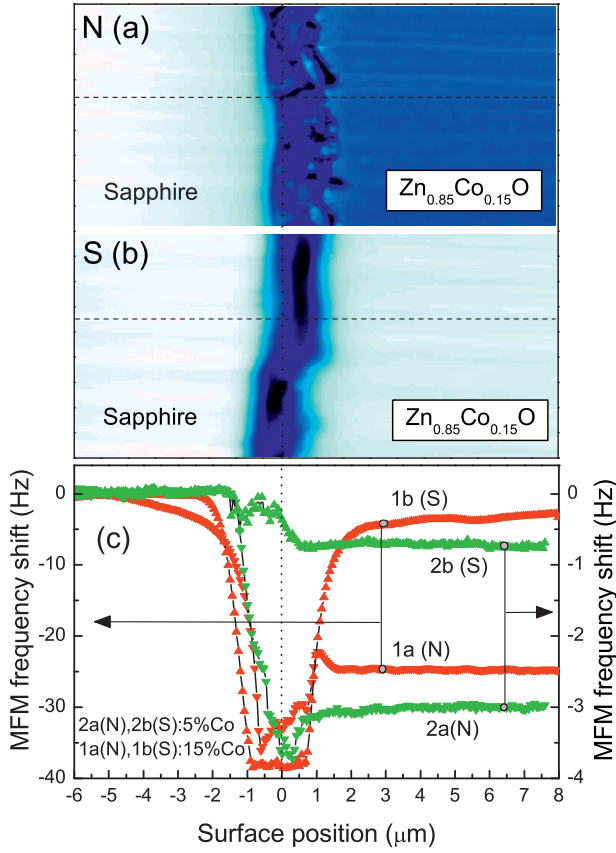
FIG. 2: MFM images at room temperature of the chipped edge of $15\%Co$-doped ZnO films scanned under North (a) and South (b) tip apex magnetization (deep blue color corresponds to higher MFM signal). Profiles of surface magnetic field gradients (c) along horizontal dashed lines on the (a) and (b) magnetic maps recorded for the North(N) and South(S) tip apex magnetization with the 15% (1a(N) and 1b(S) curves) and 5% (2a(N) and 2b(S) curves) Co-doped ZnO films.

FIG. 3: Magnetic susceptibility of the $15\%Co$-doped ZnO film (filled square) and undoped ZnO film (open circle) versus temperature at a magnetic field of $H = 1000$ Oe with $H \perp c$ geometry. The insert shows a dependence of the magnetization for the undoped ZnO film versus magnetic field at 5 (filled circles) and 300 K (open circles) for $H \perp c$ geometry.

FIG. 4: Magnetization of the $Zn_{1-x}Co_xO$ film with $x = 15\%$ versus magnetic field. $M(H)$ were taken at 5 (squares) and 300 K (circles) with $H \perp c$ (filled symbols) and $H \parallel c$ (open symbols) geometry of a magnetic field, respectively. The inserts show in more details the region near the zero field for both geometries.

of the Fig. 4). It does indicate ferromagnetic behavior at room temperature in the films.

The MFM investigations did not reveal any fine magnetic surface structure of the films even in the high resolution mode with a lift height of 10nm. The observed uniform contrast of the MFM picture can testify for homogeneous distribution of the doping Co impurity over the surface of the $Zn_{1-x}Co_xO$ alloys at least with the precision of our MFM experiments (20 nm). In the opposite case, the magnetic contrast and surface topography image would be correlated in some manner. It was observed, for instance, for $V^{2+}:ZnO$ nano-rods, when the pattern of separate vertically oriented magnetic dipoles were correlated with topographical AFM images of the nano-rods[24].

In order to study the magnetic properties of the films, we have performed SQUID measurements. It is seen from Fig. 3 that the temperature dependences for undoped and $15\%Co$-doped ZnO films drastically differ. The ob-
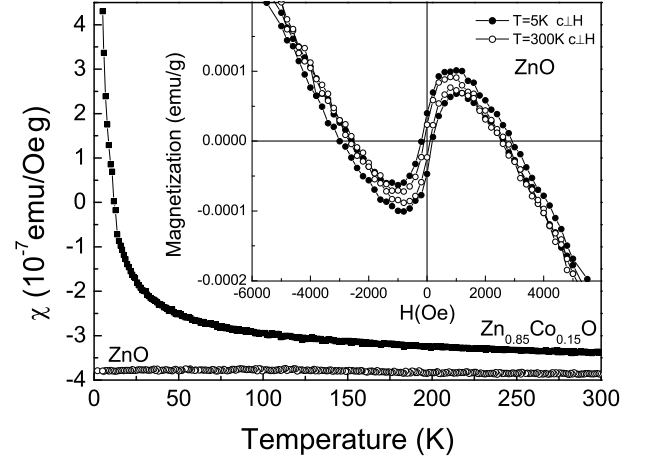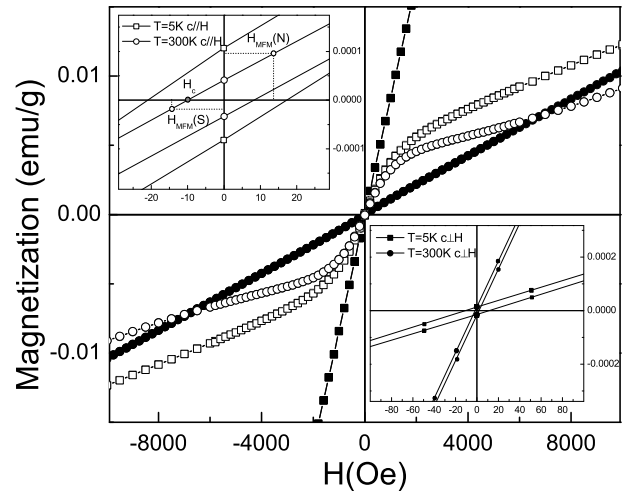
served higher value for magnetization of $15\%Co$-doped ZnO film is caused by strong interaction between Co^{2+} ions with the magnetic moment close to $3\mu_B$ per Co^{2+} ion in $Zn_{1-x}Co_xO$ film[12,19]. The magnetic susceptibility in the undoped ZnO film is negative (Fig. 3) and practically does not depend on temperature. For the $15\%Co$-doped sample one can observe a strong dependence of the magnetic susceptibility on temperature that is described with the Curie-Weiss law. The diamagnetic contribution

$\chi = C/(T - \Theta) + \chi_{sub}$, where C is the Curie constant, Θ-Curie-Weiss temperature, and χ_{sub} - diamagnetic susceptibility of substrate, were taken into account when analyzing SQUID data for the Co-doped samples. As a result, for the undoped ZnO film we obtained low magnetization values $< 0.1\mu_B$ magnetic moment per defect, which is often related with oxygen vacancies[25]. Weak ferromagnetism for undoped ZnO film is clearly demonstrated by magnetization reversal loops in the insert of Fig. 3. For the case of Co-doped ZnO films, the obtained results for magnetization are shown in Figs. 4 and 5 with account of the substrate diamagnetic contribution.

Peculiarities of hysteresis curves of the $Zn_{1-x}Co_xO$ samples are observed in magnetization measurements up to 300 K (Fig. 4). The temperature dependence of inverse magnetic susceptibility in a magnetic field of 1000 Oe is shown in Fig. 5. The magnetic susceptibility has two well distinguished temperature regimes (at low (LT) and high (HT) temperatures, respectively) with a typical Curie-Weiss behavior for both $H \perp c$ and $H \parallel c$ geometry of magnetic field. The Curie temperatures Θ obtained from extrapolation to the temperature axis show clearly the HT and LT regimes of effective magnetic interactions (Fig. 5 and Table II). As a result of the dominant ferromagnetic interactions between the Co^{2+} ions one can observed hysteresis loops with coercivity values of $H_c^\perp \approx 20$ Oe and $H_c^\parallel \approx 10$ Oe at 300 K (inserts on Fig. 4). On the other hand, at low temperature ($T < 200$ K), one obtains a negative Curie-Weiss temperatures (Fig. 5 and Table II), which can be considered as a result of antiferromagnetic behavior of $Co - O - Co$ sequences and has previously been observed for the $Zn_{1-x}Co_xO$ films[19,20] and powders[26]. So, when analyzing the magnetic properties of Co-doped ZnO films, the change in magnetic behavior of the $Zn_{1-x}Co_xO$ films can be understood as the result of a competition between the ferro- and antiferromagnetic Co interactions, which are due to isolated Co ions and $Co - O - Co$ sequences[20,21], respectively. Effective indirect exchange interaction between isolated Co^{2+} ions decreases with decreasing the carrier mobility and at low temperatures the dominant magnetic interaction is antiferromagnetic due to Co-O-Co sequences. The carrier concentration in our films is $\sim 10^{20}$ cm^{-3} at any temperature, a value obtained from the ω^+ LOPCM in the Raman spectra. Therefore for these high quality MBE-grown $Zn_{1-x}Co_xO$ films, the high-temperature ferromagnetism is expected to be due to the high electron concentration in the conduction band.

TABLE II: Values of the Curie-Weiss temperatures at magnetic field geometries of $H \perp c$ and $H \parallel c$ for of the $Zn_{1-x}Co_xO$ film with $x = 15\%$.

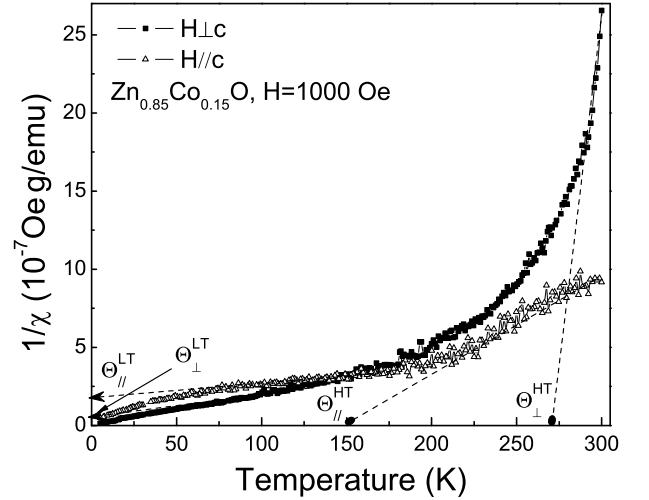| $\Theta_\parallel^{LT}$ (K)	$\Theta_\perp^{LT}$ (K)	$\Theta_\parallel^{HT}$ (K)	$\Theta_\perp^{HT}$ (K)
-200	-40	150	270

FIG. 5: Inverse magnetic susceptibility of the $Zn_{1-x}Co_xO$ film with $x = 15\%$ versus temperature at a magnetic field of $H = 1000$ Oe with $H \perp c$ (filled square) and $H \parallel c$ (open triangle) geometry.

It is well known that for $Zn_{1-x}Co_xO$ films the magnetization curves at low magnetic field, which is a more favorable for ferromagnetism observation, can be different from the prediction of the effective spin model[19] used for an interpretation of the para- and antiferromagnetic Co behaviors. For studied films, the magnetization (Fig. 4) and magnetic susceptibility (Fig. 5) curves reveal the presence of a significant magnetic anisotropy with a magnetic moment $M \perp c$ as observed in Refs.[19],[20]. The fact that $M \perp c$ is greater than $M \parallel c$ at a low temperature is in good agreement with theoretical predictions that antiferromagnetic interactions of Co-O-Co sequences are less stable than ferromagnetic interactions along the c direction[10,27]. The ferromagnetic interaction in this direction is more favorable for ferromagnetism, at least for temperature above 200 K, as observed in our SQUID measurements (Fig. 5).

Fig. 6 provides PL spectra of undoped (curve 1) and Co-doped (5 and 15%Co, curve 2 and 3, respectively) ZnO films at $T = 300K$ (in insert at $T = 6$ K). In the PL spectra of undoped ZnO films, a broad green emission band is observed at ~ 2.18 eV, which is associated with intrinsic deep-level defects in ZnO, namely: oxygen vacancies, interstitial zinc atoms, and antisite oxygen atoms[10,28]. For the 5%Co-doped ZnO, the red emission peak at ~ 1.816 eV (~ 683 nm) (Fig. 6, curve 2) corresponds to electron transitions between d-levels [29] of isolated Co^{2+} ions tetrahedrally coordinated to oxygen atoms. Increasing Co concentration to 15%, induces a red-emission weakening due to decrease of the isolated Co^{2+} ions and increase of $Co - O - Co$ sequences[8,18], which don't contribute to the red band emission. In addition, the effect of decreasing the intensity of red emission cannot be related with formation of secondary phases

such as octahedral Co oxides, since no indication of additional structure phases were observed in Raman and X-ray diffraction measurements within the detection limit.
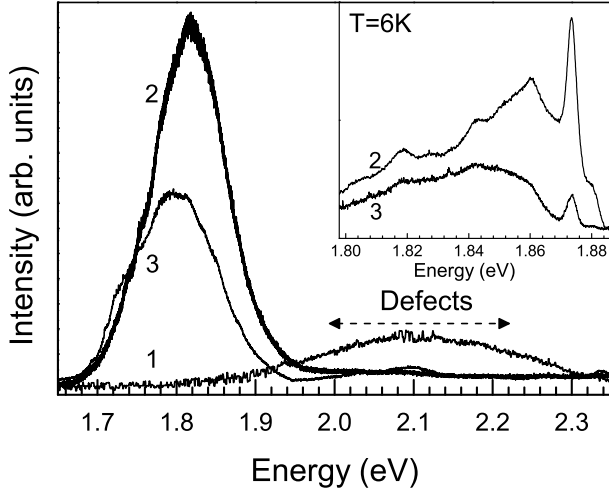

FIG. 6: PL spectra of the undoped (1), 5 and 15%Co-doped (2 and 3, respectively) ZnO films excited by $E_{exc} = 2.54 \ eV$ (488.0 nm) at $T = 300$ K and $T = 6$ K (insert).
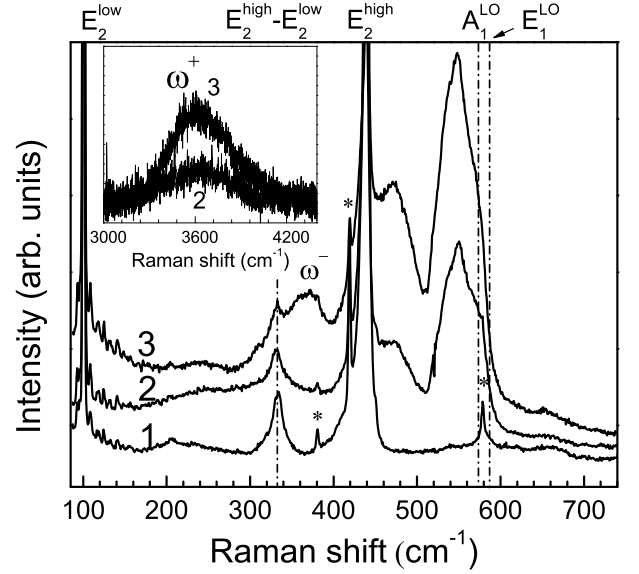

FIG. 7: Room temperature Raman spectra of undoped (1) and doped with 5 and 15%Co (2 and 3, respectively) ZnO films. $E_{exc} = 2.54$ eV. $T = 300$ K.

Raman measurements were performed to analyze the vibrational modes and lattice structure of the Co-doped ZnO films. They confirm that the films do have the wurtzite structure. Indeed, Fig. 7 exhibits micro-Raman spectra taken from an undoped (curve 1) and Co-doped (5 and 15%Co, curves 2 and 3, respectively) ZnO films. According to group theory, four Raman-active modes A_1, E_1 and $2E_2$ (E_2^{low} and E_2^{high}) are expected for the wurtzite-type ZnO structure, which belongs to the space group $P6_3mc$. The polar nature of A_1 and E_1 modes leads to a splitting into TO and LO components. The E_2^{low} and E_2^{high} modes are non-polar. In the backscattering geometry for (0001) ZnO, both E_2 and $A_1(LO)$ modes can be detected. The $A_1(LO)$ mode at ~ 574 cm^{-1} shows very low intensity for high-quality ZnO films. The most pronounced peaks in ZnO originate from E_2^{low} and E_2^{high} phonon modes at ~ 100 and ~ 437 cm^{-1}, respectively. The E_2^{high}-E_2^{low} modes are observed at ~ 333 cm^{-1}. Fig. 7 illustrates also the presence of three phonon modes of the sapphire substrate (denoted asterisks) with the A_{1g} (418 cm^{-1}) and E_g (379 and 578 cm^{-1}) symmetries, respectively.

The Raman non-polar E_2^{low} and E_2^{high} modes in undoped ZnO films are very sensitive to disorder in zinc and oxygen sublattices, respectively. According to Fig. 7 (curve 1), for undoped ZnO films the E_2^{low} mode at ~ 100.5 cm^{-1}, involving mainly Zn motion, displays a very narrow linewidth (~ 1.6 cm^{-1}). After Co doping, the E_2^{low} mode intensity strongly decreases. The mode is broadened up to ~ 2.4 cm^{-1} and undergoes a red shift (up to ~ 0.7 cm^{-1}) with respect to undoped ZnO. It is

the effect of compositional fluctuations induced by random substitution of Co ions into Zn sites in host lattice. Such an alloying effect does not usually involve any precipitation of other crystalline phases and occurs, for example, in $(Ga, In)N$, where In-rich quantum-dot-like regions arise[30]. The spectra also exhibit an intense E_2^{high} mode associated with oxygen-atom vibrations which appears at ~ 439.5 cm^{-1} with a full-width-at half maximum $\Gamma \sim 5$ cm^{-1} for undoped ZnO film. With the increase of Co amount, the E_2^{high} mode shows a red shift up to ~ 1.2 cm^{-1} and broadens up to ~ 13 cm^{-1} due to disorder effects in the oxygen sublattice (vacancies, interstitials) inducing a change in coordination numbers of some Co atoms due to oxygen vacancies.

In the Raman spectra of most heavily doped ZnO is often observed intensity signal in region between of the TO and LO modes, the interpretation of this bands is ambiguous. For Co-doped samples, an additional overlapping broad and intensity bands in the region of 450-580 cm^{-1} are detected (Fig. 7). These bands were seen in different scattering geometries and therefore could be attributed to the ZnO phonon states due to disorder activated Raman scattering[31]. It is assumed also[32,33] that for Co-doped ZnO nanostructures a broad feature at 470-500 cm^{-1} may be assigned to the surface optical phonon mode (SOP) (Fig.Fig. 7). When the crystallite size of ZnO is $10nm < L < 100nm$, the SOP can be appear and its intensity increasing with reducing the nano-column diameter[34]. It is noteworthy that the SOP peak is reliably detected in resonant multi-phonon Raman spectra ($E_{exc} = 3.81$) of undoped and Co-doped ZnO films, the frequency of this mode being independent of the Co con-

centration (is not shown). Difficulties in SOP detection in non-resonant Raman spectra of undoped ZnO films may be due to as well with large crystalline size (150-200 nm) as considerable disordering at the boundaries of the internal grain structure, as compared with Co-doped films.

Additional bands at ~ 488, 550 and ~ 708 cm^{-1} in Co-doped bulk samples and thin ZnO films grown by various methods have been reported in the literature[17,35]. These bands arise from secondary structural phases. They can be clusters of Co_3O_4 or isometric compounds $Zn_xCo_{3-x}O_4$. However, in the present samples, additional Raman bands of these secondary phases are not present.

An intense wide band appears in the frequency range of 550-600 cm^{-1} for the Co-doped samples (Fig. 7). At least two Lorentzian profiles are necessary for fitting the band which splits into two subbands at frequencies ~ 550.8 cm^{-1} ($\Gamma \sim 33$ cm^{-1}) and ~ 576.3 cm^{-1} ($\Gamma \sim 22$ cm^{-1}) for the 5%Co and ~ 546.2 cm^{-1} ($\Gamma \sim 46$ cm^{-1}) and ~ 572.9 cm^{-1} ($\Gamma \sim 27$ cm^{-1}) for the 15%Co concentrations, respectively. It is interesting to note that with increasing Co concentration from 5 to 15%, the intensity of both modes is substantially increased. This gives a clear evidence for the Co substitution in ZnO host lattice[17]. A similar increase in the intensity of the Raman band was reported for the multiphonon mode at 540 cm^{-1} and $E_1(LO)$ mode at 584 cm^{-1} in Co-doped[17] ZnO. In our opinion, these bands are related with the resonant Raman effect at subband-gap excitation caused by d-d transitions in Co^{2+} ions as well as by defect levels in ZnO host in the energy range $2.2 - 3.0$ eV[36]. The extrinsic Fröhlich interaction mediated by the localized electronic states bounded to defect, impurities and $3d$-related levels of Co^{2+} ions could enhance the scattering efficiency independently on the phonon wave vector $\mathbf{q}$.

The zone-center LO phonons are affected by the n-type conductivity which is due to the oxygen vacancy (V_o) and interstitial $Zn(Zn_i)$[37] of the Co-doped ZnO films, since we deal with electron concentrations higher than 10^{19} cm^{-3}. In polar semiconductors, when the frequency of longitudinal plasma oscillations approaches the LO phonon frequencies, their macroscopic electric fields strongly interact, which results in appearance of the ω^- and ω^+ LOPCMs. However, owing to poor carrier mobility of the doped ZnO epilayers, it is expected that the LOPCMs are overdamped due to existence of many structural defects.

In order to assign the bands in films with 5 and 15%Co at ~ 342 cm^{-1} and ~ 368 cm^{-1}, respectively, to plasmon modes, we performed the Raman measurements at temperatures from 80 to 500 K (Fig. 8) analyzed band shapes with the help of a semiclassical theory of Raman scattering[38]. Both the electro-optic and deformation potentials (I^{DP-EO}) as well as charge-density (I^{CDF}) contributions to the processes of light scattering were taken into account. The ω^- plasma-like modes are fitted by

using the following set of equations:

$$I(\omega) = A_1 I^{DP-EO}(\omega) + A_2 I^{CDF}(\omega) =$$

$$\left(A_1 \overline{\left[\frac{\omega_{TO}^2(1+C_{FH})-\omega^2}{\omega_{TO}^2-\omega^2}\right]^2} + A_2 \overline{\left[\frac{\omega_{LO}^2-\omega^2}{\omega_{TO}^2-\omega^2}\right]^2} \right) Im\left(-\frac{1}{\epsilon(\omega)}\right),$$

$$\epsilon(\omega,\vec{q}) = \epsilon_\infty + \epsilon_\infty \frac{\omega_{LO}^2-\omega_{TO}^2}{\omega_{TO}^2-\omega^2-i\Gamma\omega} - \epsilon_\infty \frac{\omega_p^2}{\omega(\omega+i\gamma)},$$

$$\tag{1}$$

where ϵ_∞ is the high-frequency dielectric constant, C_{FH} is the Faust-Henry coefficient, ω_{LO} and ω_{TO} are frequencies of the LO and TO phonons, $\Gamma(\gamma)$ is a phonon (plasmon) damping coefficient, ω_p is a plasmon frequency.

We used the prefactors of $Im(-1/\epsilon)$ in Eq. 1 for the light-scattering efficiency from Ref.[38]. By using the optimization procedure for the ω^- plasma-like mode[39] one finds the A_1, A_2 coefficients and the γ parameter for which the sum of the chi-square value, $\sum (I^{exp}(\omega) - I(\omega))^2$ is minimal at fixed ω_p and Γ values. The ω^- band shape fitting analysis was made for each of the Raman spectra at a given temperature in order to get the plasmon damping, γ versus temperature.

Two calculated LOPCMs modes (dashed lines) are shown in Fig. 8 and demonstrate very good agreement with the experimental spectra. For modeling the ω^- LOPCM band we used the following parameter values: $C = 6.4$[40], $\omega_{TO} = 381.6$ cm^{-1} and $\omega_{LO} = 574.2$ cm^{-1}, $\epsilon_\infty = 3.67$ and the effective mass of electron $m^* = 0.27m_0$ where m0 is the electron mass in vacuum. The plasmon damping value provides the carrier mobility value ($\mu = e/m^*\gamma$), and the plasma frequency ω_p is related with the carrier concentration n by the relation $\omega_p^2 = 4\pi e^2 n/\epsilon_\infty m^*$. Therefore, one can obtain also the carrier mobility value, μ, versus temperature.

Fig. 9 shows the temperature dependence of the electron mobility for the $Zn_{1-x}Co_xO$ films with 5 and 15%Co, respectively, obtained from modeling the ω^- LOPCMs band. We found ω_p and Γ values equal to 3400 cm^{-1} and 47 cm^{-1}, respectively, at any temperature. The value of ω_p corresponds to electron concentration $\sim 1.3 \times 10^{20}$ cm^{-3}. Such large value for ω_p is in good agreement with a spectral position of the ω^+ LOPCMs ($\omega_p \approx \omega^+$) observed in the experimental Raman spectra for the $Zn_{1-x}Co_xO$ films with 5 and 15%Co (see insert in Fig. 7). The plasmon damping parameter γ has a strong temperature dependence, which arises from the temperature dependence of the electron mobility. In order to determine the influence of ferromagnetic ordering on the carrier mobility, we calculate contributions to the mobility, which are due to the carrier scattering process on the acoustic $\propto (kT)^{-3/2}$ and optic $\propto (exp(\hbar\omega_{LO}/kT) - 1)$ phonons (Fig. 9) in high quality epitaxial undoped ZnO films[37]. Even if the mobility in our $Zn_{1-x}Co_xO$ films decreases at temperature increasing up to 500 K, its value is comparable to that in structurally perfect ZnO films at temperatures around 500 K. It is interesting to note that the electron mobility in the films with 15%Co is higher than that with 5%Co at any temperature (Fig. 9). Cor-
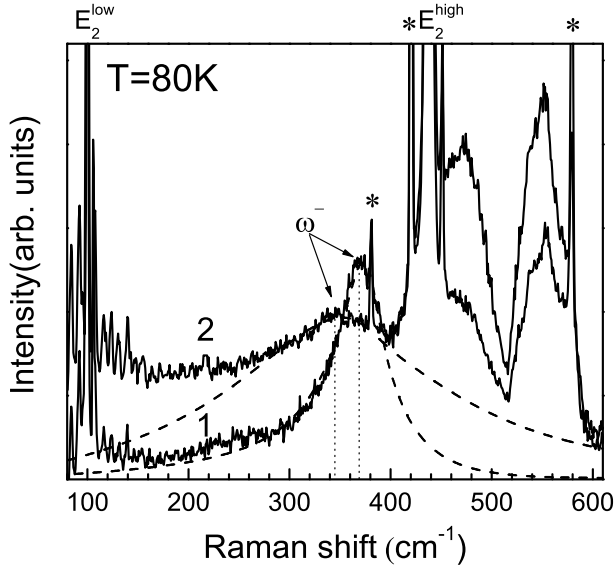
FIG. 8: Raman spectra for the $Zn_{1-x}Co_xO$ films at $80K$. The dashed lines correspond to the modelled ω^- LOPCMs band at ~ 342 and ~ 368 cm^{-1} with 5 (2) and 15%Co (1), respectively.
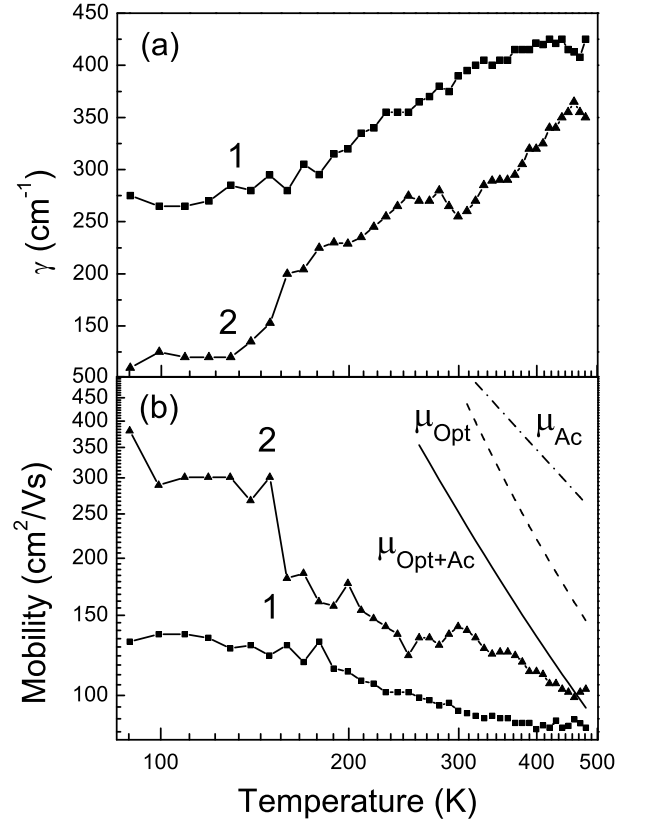

FIG. 9: Temperature dependence of the plasmon damping(a) and electron mobility(b) obtained from the analysis of Raman spectra for $Zn_{1-x}Co_xO$ films with 5% (1) and 15% (2). The solid, dashed and dot dashed lines show the dependences for the electron mobilities limited by processes of scattering on acoustic and optic phonons as well as limited by their joint contribution, respectively. $\omega_p = 3400$ cm^{-1}. $\Gamma = 47$ cm^{-1}.

relation between magnetic and transport properties was published for DMS based on A^3B^5 semiconductors[41]. For example, for p-$GaMnAs$ the maximum value of Curie temperature ($T_c = 110$ K) was obtained for a metallic type conductivity and with a higher value of the charge carrier mobility[41]. Such correlation between magnetic properties and electron mobility takes place in the studied $Zn_{1-x}Co_xO$ films, too (Fig. 9).

Up to now the physical mechanism of ferromagnetic ordering in n-type $Zn_{1-x}Co_xO$ is not ascertained yet. One can offer the following microscopic mechanism of ferromagnetism for the electron concentration put into evidence in the conduction band. The mechanism foresees long-range interaction between two localized magnetic moments $\vec{S}_i$ and $\vec{S}_j$ of isolated $Co^{2+}(S = 3/2)$ ions at a distance of $|\vec{R}_i - \vec{R}_j|$ via free electrons in the conduction band. For these magnetic moments, an important role is plaid by the parameter of exchange interaction J_{ij} that can oscillate in the direct space, as for $RKKY$ interaction mechanism[41,42]. The exchange interaction $J(|\vec{R}_i - \vec{R}_j|)$, which is responsible for the Curie temperature, depends on the electronic subsystem of $Zn_{1-x}Co_xO$ semiconductor[42]. For the samples to be ferromagnetic, most of the Co-atom spins should be parallel one to another. In other words, the symmetry of the total system including the crystalline lattice and Co-atom spins should be higher in the ferromagnetic phase.

Since the symmetry of the total system for the ferromagnetic phase is maximal, one should expect larger electron mobility than for a disordered configuration. However, the situation is more complex for studied anisotropic wurtzite Co-doped ZnO films. There takes place considerable anisotropy of magnetization with the easy-axis magnetization $H \perp c$[12,19] (Fig. 4). For ferromagnetic phase of Co-doped ZnO films ($H \perp c$, $T > 40K$, Table II), we performed the analysis of Raman spectra of LOCPMs and found an increase of the carrier mobility at decreasing temperature (Fig. 9). This effect could be explained by phonon mechanism of the carrier scattering[37]. Note that the carrier mobility (and magnetization) is higher for 15% sample as compared with 5% sample (Fig. 9). It remains to explain why ferromagnetism takes place only at rather high temperatures. One can suggest that coupling between electron spins and Co-atom spins is favored by collisions with phonons. Phonon population increases with temperature which increases collision probability.

IV. SUMMARY AND OUTLOOKS

In this work, we have studied magnetic, structural, optical and electronic properties of high quality MBE-grown $Zn_{1-x}Co_xO$ films with $x = 0$ (undoped), $x = 5\%$ and $x = 15\%$. We provide experimental evidence for important role of electrons, which rise ferromagnetism properties up to room temperature.

From MFM magnetization maps and SQUID measurements, ferromagnetic behavior of films at room temperature is clearly put into evidence. SQUID data show a complicated temperature dependence of the magnetic susceptibility, which is due to two different kinds of coordination, at the range of second first neighbors, for Co^{2+} ions within the ZnO host. $Co - O - Co$ sequences contribute to antiferromagnetic behavior whereas isolated Co^{2+} ions contributes to ferromagnetic properties of the films. High temperature ferromagnetism results from interaction between isolated ions at cation sites mediated by conduction electrons (RKKY-like mechanism). On the contrary, at low temperatures (temperatures below $150K$), the antiferromagnetic effect of $Co - O - Co$ sequences is dominant.

The Raman measurements confirm the high crystalline quality of both undoped and Co-doped ZnO films as well as their wurtzite structure. Raman bands of the antiferromagnetic Co oxygen spinel clusters have not been observed. The red Co emission exhibit a broad peak at 1.816 eV (683 nm), which can be ascribed to electron transitions within isolated Co^{2+} ion.

Raman investigation of LOPCMs versus temperature has been used to probe the free-carrier properties in films. A modeling of the ω^- LOPCMs band was performed which allows determining the temperature dependence of the charge carrier mobility. Curie temperature increases with Co concentration from 5% to 15%, and the magnetic films with a higher value of the magnetisation have a higher electron mobility.

V. ACKNOWLEDGMENTS

[1] T. Dietl, H. Ohno, F. Matsukura, J. Cibert, and D. Ferrand, Science **287,**, 1019 (2000).

[2] H. Saeki, H. Tabata, and T. Kawai, Solid State Commun. **120,** 439 (2001).

[3] S.-J. Han, J.W. Song, C.-H. Yang, S. H. Park, J.-H. Park,Y. H. Jeong, and K.W. Rhie, Appl. Phys. Lett. **81,** 4212 (2002).

[4] K. Ueda, H. Tabata, and T. Kawai, Appl. Phys. Lett. **79,** 988 (2001); K. Rode, A. Anane, R. Mattana, J.-P.Contour, O. Durand, and R. LeBourgeois, J. Appl.Phys. **93,** 7676 (2003).

[5] Key Potzger and Shengqlang Zhou, Phys. Stat. Sol. (b) **246,** 1147 (2009).

[6] M. Snure, D. Kumar, and A. Tiwari, Appl. Phys. Lett. **94,** 012510 (2009). S. K. Mandal, A. K. Das, T. K. Nath, D. Karmakar, and B. Satpati, J. Appl. Phys. **100,** 104315 (2006). C.N.R. Rao, F.L. Deepak, J. Mater. Chem. **15,** 573 (2005).

[7] A. Kaminski and S. Das Sarma, Phys. Rev. Lett. **88,** 247202 (2002).

[8] Scott Chambers, Adv. Materials **22,** 219 (2010).

[9] Xuefeng Wang, J. B. Xu, and Ning Ke, Jiaguo Yu , Juan Wang, Quan Li, and H.C. Ong, R. Zhang, Applied Phys. Lett. **88,** 223108 (2006). P.V. Radovanovic and D.R. Gamelin, Phys. Rev. Lett. **91,** 157202 (2003).

[10] S. B. Zhang, S.-H. Wei, and A. Zunger, Phys. Rev. B **63,** 075205 (2001).

[11] K.R. Kittilstved, N.S. Norberg, and D.R. Gamelin, Phys. Rev. Lett. **94,** 147209 (2005).

[12] P. Sati, R. Hayn, R. Kuzian, S. Regnier, S. Schafer, A. Stepanov,C. Morhain, C. Deparis, M. Laugt, M. Goiran, Z. Golacki, Phys. Rev. Lett. **96,** 017203 (2006).

[13] K.R. Kittilstved, D.A. Schwartz, A.C. Tuan, S.M. Heald, S.A. Chambers,D.R. Gamelin, Phys. Rev. Lett. **97,** 037203 (2006).

[14] Shinji Kuroda, Nozomi Nishizawa, Kôki Takita, Masanori Mitome, Yoshio Bando, Krzysztof Osuch and Tomasz Dietl, Nature Materials **6,** 440 (2007).

[15] C. Bundesmann, N. Ashkenov, M. Schuber, D. Spemann, T. Butz, E.M. Kaidashev, M. Lorents and M. Grundmann, Appl. Phys. Lett. **83,** 1974 (2003), N.H. Nickel, F. Friedrich, J.F. Rommeluère and P. Faltier, Appl. Phys. Lett. **87,** 211905 (2005).

[16] C. Sudakar, P.Kharel, G. Lawes, R. Suryanarayanan, R. Naik, and V. M.Naik, J. Phys.: Cond. Mat. **19,** 026212 (2007).

[17] K. Samanta, P. Bhattacharya, R.S. Katiyar, W. Iwamoto, P.G. Pagliuso and C. Rettori, Phys. Rev. B **73,** 245213 (2006).

[18] A. Ney, K. Ollefs, S. Ye, T. Kammermeier, V. Ney, T.C. Kaspar, S.A. Chambers, F. Wilhelm, A. Rogalev, Phys. Rev. Lett **100,** 157201 (2008).

[19] P. Sati, S. Schäfer, C. Morhain, C. Deparis, A. Stepanov, Superlattices and Microstructures **42,** 191 (2007).

[20] A. Ney, T. Kammermeier, K. Ollefs, S. Ye, and V. Ney, T.C. Kaspar and S.A. Chambers, F. Wilhelm and A. Rogalev, Phys. Rev. B **81,** 054420 (2010).

[21] M. Kobayashi, Y. Ishida, J.I. Osafune, A. Fujimori, Y. Takeda, T. Okane, Y. Saitoh, K. Kobayashi, H. Saeki, T. Kawai, and H. Tabata, Phys. Rev. B **81,** 075204 (2010).

[22] X.J. Liu, C. Song, F. Zeng, F. Pan, B. He, W.S. Yan, J. Appl. Phys. **103,** 093911 (2008).

[23] B.Z. Dong, G.J. Fang, J.F. Wang, W.J. Guan, and X.Z. Zhao, J. Appl. Phys. **101,** 033713 (2007).

[24] E. Schlenkera, A. Bakin, B. Postels, A.C. Mofora, M. Kreye, C. Ronningb, S. Sieversc, M, Albrecht, U. Siegner, R.

Kling, A. Waag, Superlattices and Microstructures **42,** 236 (2007).

[25] Q. Wang, Q. Sun, G. Chen, Y. Kawazoe, and P. Jena, Phys. Rev. B 77, 205411 (2008).

[26] A.S. Risbud, N.A. Spaldin, Z.Q. Chen, S. Stemmer, and Ram Seshadri, Phys. Rev. B **68,** 205202 (2003).

[27] Eun-Cheol Lee and K.J. Chang, Phys. Rev. B **69,** 085205 (2004).

[28] J.M.D. Coey, M. Venkatesan, and C. B. Fitzgerald, Nat. Mater. **4,** 173 (2005),

[29] P. Lommens, P.F. Smet, C. de Mello Donega, A. Meijerink, L. Piraux, S.Michotte, S. Matefi-Tempfli, D. Poelman, and Z. Hens, J. Lumin. **118,** 245 (2006).

[30] V.Yu. Davydov, I.N. Goncharuk, A.N. Smirnov, A.E. Nikolaev, W.V. Lundin, A.S. Usikov, A. A. Klochikhin, J. Aderhold, J. Graul, O. Semchinova, and H. Harima, Phys. Rev. B **65,** 125203 (2002).

[31] J. Serrano, A.H. Romero, F.J. Manjón, R. Lauck, M. Cardona, and A. Rubio, Phys. Rev. B **69,** 094306 (2004).

[32] P.-M. Chassaing, F. Demangeot, V. Paillard, A. Zwick, N. Combe, C. Pags, M. L. Kahn, A. Maisonnat, and B. Chaudret, Phys. Rev. B **77,** 153306 (2008).

[33] F.A. Fonoberov, A.A. Balandin, Phys. Rev. B **70,** 233205 (2004).

[34] S. Hayashi and H. Kanamori, Phys. Rev. B **26,** 7079 (1982), K.W. Adu, Q. Xiong, H.R. Gutierrez, G. Chen, P.C. Eklund, Appl. Phys. A **85,** 287 (2006).

[35] Y. Liu and J.L. MacManus-Driscoll, Appl. Phys. Lett. **94,** 022503 (2009).

[36] N. Hasuike, K. Nishio, H.Katoh, A. Suzuki, T. Isshiki, K.Kisoda, H. Harima, J. Phys.: Condens. Matter **21,** 064215 (2009).

[37] Klaus Ellmer, Andreas Klein, Bernd Rech, Transparent Conductive Zinc Oxide. Basic and Applications in Thin Film Solar Cells, Springer-Verlag Berlin pp.443 (2008) ISBN: 978-3-540-73611-0.

[38] G. Irmer, M. Wenzel, and J. Monecke, Phys. Rev. B **56,** 9524 (1997).

[39] V.V. Strelchuk, V.P. Bryksa, M.Ya. Valakh, K. Avramenko and A.E. Belyaev, Phys. Rev. B in press

[40] B.H. Bairamov, A. Heinrich, G. Irmer, V.V. Toporov and E. Ziegler, Phys. Stat. Sol. (b) **119,** 227 (1983).

[41] T. Jungwirth, Jairo Sinova, J. Masek, J. Kucera, A.H. MacDonald, Rev. Mod. Phys. **78,** 809 (2006).

[42] V. Bryksa, W. Nolting, Phys. Rev. B **78,** 064417 (2008).